Published in "Physical Review A 75: 042505, 2007"
which should be cited to refer to this work.

Measurement of the forbidden electric tensor polarizability of Cs atoms trapped in solid ^{4}He

S. Ulzega,* A. Hofer, P. Moroshkin, R. Müller-Siebert,† D. Nettels,‡ and A. Weis
Département de Physique, Université de Fribourg, Chemin du Musée 3, 1700 Fribourg, Switzerland§

We have measured the electric tensor polarizabilities of the hyperfine levels of Cs atoms embedded in a body-centered cubic ^{4}He crystal. The polarizabilities are inferred from the shift of optically detected magnetic resonance lines in each hyperfine level induced by static electric fields up to 50 kV/cm. We recorded the magnetic resonances both by scanning the rf frequency and in a configuration in which the system is operated as a phase-stabilized magnetometer. The results from both measurements agree well with model calculations taking the effect of the solid helium matrix and our recent extension of the theory of forbidden tensor polarizabilities into account. We have also performed the first measurement of the differential tensor Stark splittings of the $F=3$ and $F=4$ hyperfine levels of the ground state, thus confirming the recently revised sign of this shift which affects the blackbody correction of primary frequency standards.

I. INTRODUCTION

The Stark effect, i.e., the effect of a static electric field on atomic properties is one of the fundamental interactions in atomic physics. In this paper we address tiny modifications of the energy of the magnetic sublevels of the cesium ground state induced by the tensor part of the electric interaction.

The Stark effect of the atomic hyperfine structure was treated in a comprehensive paper by Angel and Sandars [1] who showed that in second order perturbation theory the Stark shift of a level $|\gamma\rangle=|nL_J,F,M\rangle$ can be parametrized in terms of scalar, $\alpha_0^{(2)}$, and tensor, $\alpha_2^{(2)}$, polarizabilities. As tensor polarizabilities have nonzero values for states with $L \geqslant 1$ only, the spherically symmetric $nS_{1/2}$ ground state of alkali atoms has only a scalar polarizability and all its magnetic sublevels $|F,M\rangle$ are expected to experience the same Stark shift, independent of F and M. However, it has been experimentally known since several decades that an electric field leads to F-dependent [2] and M-dependent [3] energy shifts in the alkali ground states. The latter effect is described by a (forbidden) tensor polarizability α_2. Improved measurements of the ground state tensor polarizabilities were performed by Carrico *et al.* [4] and Gould *et al.* [5] using conventional atomic beam Ramsey resonance spectroscopy. A recent remeasurement of the tensor polarizability of ^{133}Cs in an all optical atomic beam experiment [6] has confirmed the earlier experimental values [4,5] of $\alpha_2(F=4)$ of cesium.

In 1967 Sandars [7] showed that the F- and M-dependence of the Stark effect can be explained by extending the perturbation theory to third order after including the hyperfine interaction. The theoretical expression for the tensor polarizability $\alpha_2^{(3)}(F=4)$ given in [7] was evaluated numerically in [3,5] under simplifying assumptions. The comparison with the experimental polarizabilities showed that the absolute theoretical values were systematically larger for all five alkalis studied in [5]. We note that in cesium the third order Stark splittings of the Zeeman levels due to $\alpha_2^{(3)}$ are approximately seven orders of magnitude smaller than the overall shift of the ground state due to the second order polarizability $\alpha_0^{(2)}$.

In a recent paper [8] we have revisited the third order Stark theory by identifying and evaluating contributions which were not included in the earlier calculations. This led to a theoretical value of the tensor polarizability of Cs which is in good agreement with all existing experimental results [4–6]. As described in [8] we have also identified a sign error in the previous treatment [7] of the Stark effect concerning the relative signs of the tensor polarizabilities of the two ground state hyperfine levels. We have shown that this relative sign has a direct implication for the precise evaluation of the blackbody radiation shift of the hyperfine transition frequency from static Stark shift measurements [8].

The initial motivation for our experimental [6] and theoretical [8] studies of the third order Stark interaction was the long standing discrepancy between experimental and theoretical values of $\alpha_2^{(3)}$. With our revised theory [8] this 40-year-old problem has found a satisfactory solution. In the work reported here we have extended the study of strongly suppressed Stark interactions to cesium atoms trapped in a solid ^{4}He matrix. We have measured (and calculated) the tensor polarizability of Cs in a quantum solid matrix using two independent experimental techniques. Both methods yield consistent values of the tensor polarizability $\alpha_2^{(3)}$ whose moduli are approximately 10% larger than $|\alpha_2^{(3)}|$ of the free cesium atom. A calculation [9] which considers the influence of the helium matrix on the atomic energies and wave functions entering the third order perturbation theory can account for this matrix-induced shift. In addition we have made the first experimental determination of the relative sign and magnitude of the tensor polarizabilities of the two ground state hyperfine levels and thereby confirmed the sign predicted by our model calculations.

The extension of the Stark effect investigations to solid helium was motivated by our past proposal [10,11] that alkali

*Present address: EPFL, Lausanne, Switzerland. Email address: simone.ulzega@epfl.ch
†Present address: SELFRAG AG, Langenthal, Switzerland.
‡Present address: Biochemisches Institut, Universität Zürich, Switzerland.
§www.unifr.ch/physics/frap/

atoms in condensed helium matrices might be an interesting sample to search for a permanent electric dipole moment (EDM) of the electron. In such experiments the quadratic Stark shift constitutes a strong background and its (imperfect) suppression is a major source of systematic uncertainty. While the perturbation of optical and magnetic properties of alkali atoms by condensed (superfluid and solid) ^{4}He matrices has been studied extensively in the past decade [12] the effect of the solid He environment on static electric properties has never been addressed. To our knowledge the present study is the first investigation of the Stark effect of atomic defects in condensed helium. The study confirms that the so-called extended bubble model is well-suited for the quantitative description of such matrix-induced perturbations of electric polarizabilities.

II. THEORY

The perturbation of the energies of ground state magnetic sublevels $|\gamma\rangle = |6S_{1/2}, F, M\rangle$ by a static electric field $\mathbb{E}$ is conventionally parametrized in terms of an electric polarizability $\alpha(\gamma)$ according to

$$\Delta E(\gamma) = -\frac{1}{2}\alpha(\gamma)\mathbb{E}^2. \tag{1}$$

The polarizability $\alpha(\gamma) = \alpha^{(2)}(\gamma) + \alpha^{(3)}(\gamma)$ has contributions from perturbations arising in second and third order perturbation theory. The second order polarizability $\alpha^{(2)}$ gives rise to the well-studied scalar, i.e., F- and M-independent shift of the levels. The total third order polarizability can be written as [8]

$$\alpha^{(3)}(6S_{1/2}, F, M) = \alpha_0^{(3)}(6S_{1/2}, F) + \alpha_2^{(3)}(6S_{1/2}, F)\frac{3M^2 - F(F+1)}{2I(2I+1)}f(\theta), \tag{2}$$

where the function $f(\theta) = 3\cos^2\theta - 1$ describes the orientation of the electric field with respect to the quantization axis, and where I is the nuclear spin. The first term of Eq. (2), $\alpha_0^{(3)}$, is an F-dependent scalar contribution to the third order polarizability. It gives the main contribution to the Stark shift of the hyperfine transition frequency (F-dependent effect) but does not alter the Zeeman substructure of the ground state. The second term, described by the third order tensor polarizability $\alpha_2^{(3)}$, produces F- and M^2-dependent energy shifts. Its main effect is the removal of the Zeeman degeneracies between the magnetic sublevels within each of the two ground state hyperfine levels (M^2-dependent effect). The tensor term, evaluated for $M = 0$, also gives an additional small contribution ($\approx 1\%$) to the shift of the hyperfine transition frequency. A straightforward way to measure the effect of the tensor polarizability is the observation of an electric field induced shift of magnetic resonance transition frequencies within a given hyperfine multiplet. Because of the selection rules magnetic resonances can only be driven between adjacent magnetic sublevels $|F, M\rangle \rightarrow |F, M-1\rangle$. For Cs ($I = 7/2$) the differential Stark shift of that transition can be calculated from Eqs. (1) and (2) to be

$$\Delta\nu_{(|F,M\rangle \rightarrow |F,M-1\rangle)} = -\frac{3}{56}\frac{\alpha_2^{(3)}(F)}{h}(2M-1)\mathbb{E}^2. \tag{3}$$

The third order polarizabilities involve both the dipole-dipole and the electric quadrupole hyperfine interactions, so that $\alpha_2^{(3)}$ of the two hyperfine levels $F = 3, 4$ can be expressed [8] in terms of these contributions as

$$\alpha_2^{(3)}(F=4) = a_1 + a_2, \tag{4a}$$

$$\alpha_2^{(3)}(F=3) = -a_1 + \frac{5}{3}a_2, \tag{4b}$$

where a_1 and a_2 are due to the dipole-dipole and to the quadrupole interaction, respectively. The latter contribution is very small ($a_2/a_1 \approx 4 \times 10^{-4}$) and can be neglected. With this approximation the tensor polarizabilities of the two ground state hyperfine levels are thus connected by the simple relation $\alpha_2^{(3)}(3) \approx -\alpha_2^{(3)}(4)$. This result is in contradiction with an earlier work [7] which predicts the same sign for the tensor polarizabilities of the two ground state hyperfine levels. All measurements of tensor polarizabilities published to date were performed in the $F = I + 1/2$ hyperfine states, so that no prior experiment was sensitive to the relative signs of $\alpha_2^{(3)} \times (3)$ and $\alpha_2^{(3)}(4)$. Below we will present experimental evidence for the correctness of the sign derived in our calculation.

III. EXPERIMENTAL METHODS

A. Helium matrix isolation spectroscopy

Alkali atoms embedded in the isotropic body-centered cubic (bcc) phase of ^{4}He impose their symmetry on the local matrix environment thereby forming spherically symmetric cavities (atomic bubbles). The isotropy of the trapping sites, together with the diamagnetic nature of the matrix lead to longitudinal spin relaxation times T_1 of 1 to 2 s [13]. This allows the efficient optical pumping of the sample and the observation of magnetic resonance linewidths below 20 Hz in optical-rf double resonance experiments [14]. Moreover, condensed helium has an electric breakdown voltage in excess of 100 kV/cm, which makes it, in principle, an ideal environment for high resolution magnetic resonance experiments in strong electric fields.

B. The sample cell

The measurements reported below were performed on cesium atoms implanted in a solid ^{4}He matrix. The experimental setup is similar to the one described in [15]. The helium crystal is grown at pressures around 30 bar in a cubic copper pressure cell (inner volume = 175 cm^3) immersed in superfluid helium cooled to 1.5 K by pumping on the helium bath. Optical access to the inner cell volume is given by four lateral windows and a top window. Laser excitation and fluorescence detection of the atoms occur through the side windows, while the top window is used for the implantation process. The host matrix is doped with cesium atoms by means of laser ablation with a pulsed, frequency-doubled

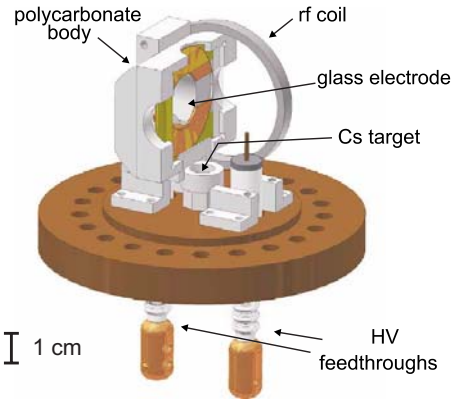

FIG. 1. (Color online) The bottom flange of the pressure cell with one of the two rf-field coils and one of the two HV electrodes shown.

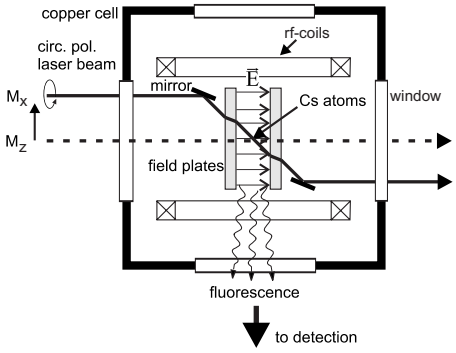

FIG. 2. Top view of the setup for magnetic resonance experiments with electric fields. The presence of two mirrors in the pressure cell allows us to switch between the M_x and M_z configurations with a simple translation of the laser beam.

Nd:YAG laser beam (2 Hz repetition rate) focused onto a solid Cs target located at the bottom of the cell. Diffusion of the implanted atoms and the subsequent binding into dimers and clusters leads to a drop of the atomic fluorescence signal with time. Low-energy pulses of the same Nd:YAG laser at a lower repetition rate are therefore used, once the crystal is doped, to dissociate dimers and clusters. In this way the average atomic density can be kept at a level of 10^8 to 10^9 cm^{-3}.

The pressure cell is surrounded by three orthogonal pairs of superconducting Helmholtz coils for applying a static magnetic field and for compensating residual fields, while another pair of Helmholtz coils mounted inside of the cell allows the application of an oscillating rf field for driving the magnetic resonance transitions (Fig. 2). The cryostat is shielded from laboratory fields by a three-layer μ-metal shield.

The inner part of the cell, shown in Fig. 1, contains a split polycarbonate body which holds the rf coils as well as two transparent glass electrodes which allow the application of the static electric field for the Stark effect experiments. The electrodes are (4 mm thick) quadratic float glass plates of 40×40 mm^2 whose facing surfaces are coated with a conductive tin oxide layer. Their opposite surfaces are partially coated with gold and electrically connected to the front surface by a vapor deposited gold stripe. Copper rings connected directly to low-temperature compatible high voltage (HV) feedthroughs containing no magnetic components are mechanically pressed onto the plates' back surfaces. The use of two feedthroughs allows us to charge each plate individually. The plate spacing of $d=6$ mm at room temperature expands to $d=6.35(5)$ mm when the cell is cooled to 1.5 K. With the given plate spacing ratio the field in the center deviates by much less than 1% from V/d.

The high voltage was generated by two identical power supplies of opposite polarities and delivered to the feedthroughs via HV cables traversing the top flange of the cryostat and the helium bath. In this way we were able to apply electric fields up to 50 kV/cm. This upper limit was due to sparking which occurred both inside and outside of the pressure cell. The doping of the crystal by laser ablation produces atomic ions and charged clusters that lead to a leakage current of a few μA (at 25 kV) between the electrodes which locally melts the crystal and limits the maximum useful voltage.

A top view of the pressure cell for magnetic resonance experiments with electric fields is shown in Fig. 2. The use of two suitably oriented mirrors allowed the easy switching between the M_z configuration ($\hat{k}=\hat{\mathbb{E}}$) and the M_x configuration ($\hat{k}\hat{\mathbb{E}}=1/\sqrt{2}$) described below by a simple horizontal translation of the laser beam.

C. The magnetic resonance technique

Optically detected magnetic resonance (ODMR) combines magnetic resonance with optical preparation and detection. It is a powerful method for performing magnetic resonance spectroscopy in dilute samples of paramagnetic atoms. A high degree of spin polarization is an essential prerequisite for observing magnetic resonance. In our experiments spin polarized cesium atoms are prepared by optical pumping [15] with circularly polarized laser light tuned to the D_1 line ($6S_{1/2}\rightarrow6P_{1/2}$ transition). Due to the large homogeneous linewidth of the optical absorption line of Cs in condensed helium [12], the hyperfine structure of the transition is not resolved. After a number of absorption-emission cycles the majority of the atoms is pumped into the state $|F=4,M=4\rangle$ which does not absorb circularly polarized light. The polarized sample thus does not fluoresce and the sample is said to be in a *dark state*. Any subsequent depolarizing interaction, such as a magnetic resonance transition, leads to an increase of the fluorescence rate. This constitutes the basis of the optical detection of the magnetic resonance. Efficient optical pumping of alkali atoms embedded in the isotropic bcc phase of solid ^{4}He was demonstrated by Lang *et al.* [15].

The optical properties of the polarized sample depend on the orientation of the spin polarization with respect to the light beam. The magnetic resonance is driven by a weak oscillating magnetic field (called rf field below) applied perpendicularly to the main static field. When the oscillation frequency coincides with the Larmor precession frequency depolarizing transitions between adjacent sublevels are induced. This leads to a resonant change in the fluorescence

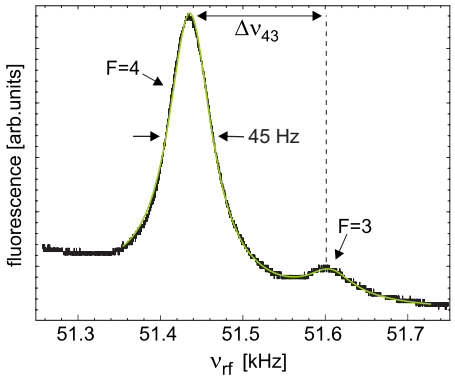

FIG. 3. (Color online) Magnetic resonances of the Zeeman transitions within the $F=4$ (left) and $F=3$ (right) hyperfine multiplets recorded with $\mathbb{E}=0$ in the M_z geometry.

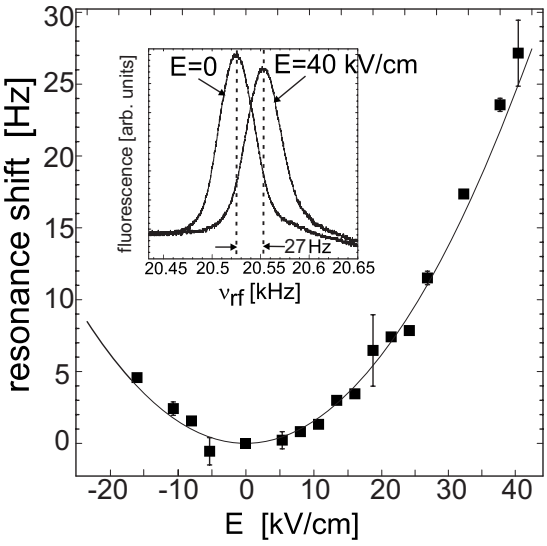

FIG. 4. Stark shift of the Cs ground state magnetic resonance $|4,4\rangle \rightarrow |4,3\rangle$ in solid ^{4}He measured in the M_z geometry. Some points have an error bar smaller than the symbol size. The fit function is of the type $\Delta\nu_4 = \eta_z \mathbb{E}^2$. The different error bars are explained in Sec. IV C. The inset shows magnetic resonance lines measured with and without applied electric field used to infer the Stark shift.

rate when the rf frequency is tuned across the Larmor frequency. In practice the same laser beam that produces the spin polarization also detects its alteration by the magnetic resonance process. The laser-induced atomic fluorescence is imaged onto an avalanche photodiode, whose photocurrent is recorded by a digital oscilloscope. Background radiation from scattered laser light is suppressed by an interference filter.

IV. MEASUREMENTS

A. The tensor polarizability in the M_z geometry

The M_z geometry is characterized by the static magnetic field $\vec{B}_0$ being oriented parallel to the propagation direction $\hat{k}$ of the pumping light and hence to the initially created spin polarization. In this case the magnetic resonance manifests itself as a resonant change of the dc level of the fluorescence signal.

The optical pumping process produces population imbalances between the magnetic sublevels in both hyperfine levels of the ground state. Because of the finite nuclear magnetic moment, the gyromagnetic ratios $\gamma(F)$ of these two states differ slightly, besides having opposite signs. As a consequence, the magnetic resonance transitions in the $F=3$ and $F=4$ states occur at slightly different frequencies and can be resolved in a single scan of the rf field, as shown in Fig. 3. In the low magnetic fields used here the Zeeman effect is linear and all individual resonances in a multiplet of given F occur at the same frequency. The dominating components in the two lines of Fig. 3 correspond to the transitions $|4,4\rangle \rightarrow |4,3\rangle$ and $|3,3\rangle \rightarrow |3,2\rangle$. The spectrum is fitted by two Lorentzian lines superposed on a curved background $bg(\nu)$. This background is due to the slow disappearance of the atomic signal as atoms recombine into dimers and clusters. It was recorded in separate runs with no applied rf field and it is well-fitted by the empirical function $bg(\nu)=b_1 \exp[-\lambda_1 \nu] + b_2 \exp[-\lambda_2 \nu]$. When an electric field is applied the magnetic resonance lines are displaced due to the M^2-dependent (differential) Stark shift of the sublevels coupled by the rf transition. This shift is proportional to $\alpha_2^{(3)}\mathbb{E}^2$. At each value of the electric field we have recorded spectra with each field polarity, in between which a spectrum with no applied field was recorded. The latter reference measurements were necessary as we observed a slow drift of the zero electric field magnetic resonance frequency (cf. Sec. IV C), which represented the main limitation of the sensitivity of our apparatus.

The dependence of the line center of the $F=4$ resonance on the electric field strength is shown in Fig. 4. According to Eq. (3) the Stark shift of the line is given by

$$\Delta\nu_4 = \eta_z \mathbb{E}^2 = -\frac{3}{8}\alpha_2^{(3)}(4)\mathbb{E}^2, \tag{5}$$

under the assumption that the line consists only of the $|4,4\rangle \rightarrow |4,3\rangle$ transition. A quadratic fit to the data, shown as a solid line in Fig. 4, then yields the tensor polarizability

$$\alpha_2^{(3)}(4) = -4.07(20) \times 10^{-2} \frac{\text{Hz}}{(\text{kV/cm})^2}. \tag{6}$$

This value is shown as point (d) in Fig. 11. The figure also shows previous experimental values of $\alpha_2^{(3)}$ (4) obtained on free Cs atoms in atomic beam experiments together with the corresponding theoretical value [8]. Equation (6) assumes that the $F=4$ line consists only of the $|4,4\rangle \rightarrow |4,3\rangle$ transition, i.e., a 100% polarized sample. Because of the finite degree of spin polarization the recorded line contains a small admixture of the $|4,3\rangle \rightarrow |4,2\rangle$ transition. Based on the rate equation calculations described in Sec. V we find that this effect leads to an underestimation of $\alpha_2^{(3)}$ by less than 1%.

We have recently extended our calculations of the Cs tensor polarizability of free Cs atoms [8] to include the effect of the helium matrix [9]. This effect increases $\alpha_2^{(3)}$ by approximately 10%, as shown in Fig. 11. The experimental result [Eq. (6)] of the measurement in the M_z geometry is in good agreement with that theoretical calculation.

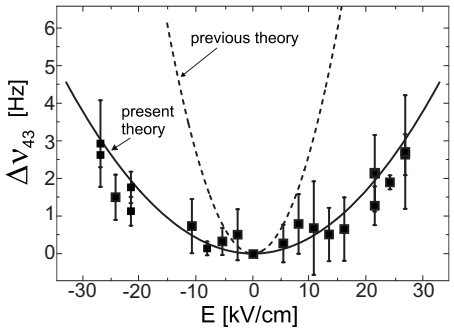

FIG. 5. The differential shift $\Delta\nu_{43} \equiv \Delta\nu_{|4,4\rangle\to|4,3\rangle} - \Delta\nu_{|3,3\rangle\to|3,2\rangle}$. The dotted line represents the prediction of Sandars' work while the solid line is the prediction of our calculations, as explained in the text.

B. The relative sign of $\alpha_2(F=4)$ and $\alpha_2(F=3)$

In order to determine the relative sign of the polarizabilities in the $F=3$ and $F=4$ states we measured the splitting $\Delta\nu_{43}$ (introduced in Fig. 3) of the corresponding resonance frequencies, defined by $\Delta\nu_{43} \equiv \Delta\nu_{|4,4\rangle\to|4,3\rangle} - \Delta\nu_{|3,3\rangle\to|3,2\rangle}$. For this measurement we use the fact that both resonances can be observed in a single scan (cf. Fig. 3). This reduces the measurement time and thus systematic effects due, e.g., to line drifts as discussed below. The line centers are inferred from Lorentzian line fits. Figure 5 shows the electric field dependence of the splitting $\Delta\nu_{43}$ between the resonances in $F=3$ and $F=4$. If one assumes $\alpha_2^{(3)}(4) = \alpha_2^{(3)}(3)$, as given in Sandars' work [7], one expects the dependence

$$\Delta\nu_{43} = -\frac{18}{28}\alpha_2^{(3)}(4)\mathbb{E}^2, \tag{7}$$

shown as a dotted line in Fig. 5. On the other hand, our recent calculation [8] predicts $\alpha_2^{(3)}(4) = -\alpha_2^{(3)}(3)$, which yields

$$\Delta\nu_{43} = -\frac{3}{28}\alpha_2^{(3)}(4)\mathbb{E}^2, \tag{8}$$

a dependence shown as a solid line in Fig. 5. The good agreement of the experimental data with the latter dependence proves that the tensor polarizabilities of the two hyperfine levels have indeed opposite signs as predicted by our calculation.

C. Line drifts

The sensitivity of the M_z configuration is limited by small instabilities of the magnetic resonance frequency (with and without applied electric field). We have made long-time recordings of the magnetic resonance signals under identical conditions and we can distinguish two distinct effects. First, on a scale of 45 min the resonance frequency shows a slow drift at a rate of 1.5–2.5 mHz/s which is equivalent to a magnetic field drift rate of about 500 fT/s. This frequency drift may also be associated with a slow motion of the center of gravity of the atomic sample due to atoms drifting in the He crystal, in combination with a magnetic field gradient. Our field has indeed a small gradient of ≈3 nT/mm [16],

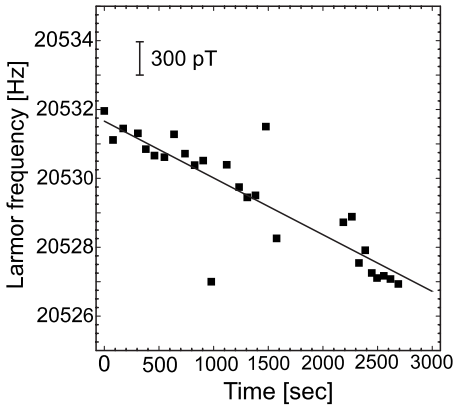

FIG. 6. Zero-electric-field resonance drift. The solid line is a linear fit which gives a drift rate of 1.7 mHz/s corresponding to a magnetic field drift of ≈500 fT/s.

corresponding to a relative inhomogeneity of 2×10^{-4}/mm. In this case the resonance drift could be explained by an atomic drift velocity of 0.2 μm/s.

A second effect occurs on a much shorter time scale. The Nd:YAG pulses, sent into the crystal every 30 s between sweeps of the rf frequency in order to dissociate clusters and to recover the optical fluorescence signal, can locally melt the crystal and occasionally provoke sudden drifts of the atoms which appear as steep jumps of their Larmor frequency (shown in Fig. 6). The error bars of Figs. 4 and 5 are related to such jumps. We determined the average of the line positions in zero field, measured before and after the actual Stark shift measurement. This average position was then subtracted from the line position measured with the field applied. In this way we could infer the Stark shift corrected for linear drifts of the baseline. The error bar reflects the drift-induced variations of the two reference measurements. The relative importance of both effects was found to vary substantially from crystal to crystal, or in a given crystal after different atomic implantations. In order to reduce such effects we have performed a second series of measurements using an alternative magnetic resonance technique described in the next section.

D. The tensor polarizability in the M_x geometry

The M_x geometry is characterized by the static magnetic field $\vec{B}_0$ being oriented at an angle β with respect to $\hat{k}$. In this case the magnetic resonance leads to a modulation of the transmitted laser power at the rf frequency with an amplitude varying as $\sin 2\beta$. The largest signal is thus obtained for $\beta = \pi/4$ (Fig. 2). In practice the modulation amplitude, which is resonant when the rf frequency matches the Larmor frequency, is measured using a phase sensitive (lock-in) amplifier referenced to the rf frequency [14]. The in-phase and quadrature components of the demodulated signals have absorptive and dispersive Lorentzian line shapes and the phase φ of the signal modulation is given by

$$\tan\varphi = \frac{\delta\nu}{\Delta\nu}, \tag{9}$$

where $\delta\nu = \nu_{rf} - \nu_L$ is the detuning of the rf frequency ν_{rf} with respect to the Larmor frequency ν_L, and where $\Delta\nu$ is the

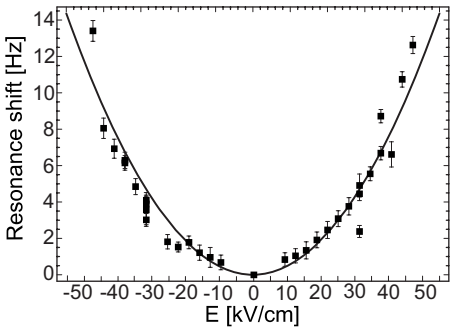

FIG. 7. Stark shift of the Larmor frequency in the M_x configuration, measured using the M_x (self-oscillating) magnetometer configuration discussed in the text. The solid line is a fit function of the type $\Delta\nu_4 = \eta_x \mathbb{E}^2$.

linewidth. The linear dependence of the phase signal $\varphi(\nu_{rf})$ near resonance ($\delta\nu \approx 0$) was used in a feedback system generating the rf frequency: the phase signal, amplified by a proportional-integral-derivative (PID) controller, was used to drive a voltage controlled oscillator which generated the oscillating voltage driving the rf coils. In this way the rf frequency was phase-locked to the Larmor frequency. Any changes of the resonance condition, induced, e.g., by a drift of the magnetic field or by a displacement of the resonance frequency induced through the Stark effect can then be detected by a real-time monitoring of ν_{rf} with a frequency counter.

This operation of the system as a phase-locked magnetometer [17] has allowed us a faster measurement of the electric field induced changes of the Larmor frequency. Compared to the experiments in the M_z geometry it has the advantage of being less sensitive to systematic effects coming from slow drifts of system parameters. It has the drawback that the resonance frequencies in the $F=3$ and $F=4$ states cannot be measured simultaneously. We have used this method to record the quadratic electric field dependence of the resonance frequency in the $F=4$ state. The results are shown in Fig. 7. A quadratic fit of the type $\Delta\nu_4 = \eta_x \mathbb{E}^2$ yields

$$\eta_x = 0.469(30) \times 10^{-2}\ \text{Hz/(kV/cm)}^2. \tag{10}$$

In the M_z geometry, in which the pumping direction is along the magnetic field (quantization axis) the field stabilizes the polarization created by optical pumping and for a 100% polarized sample the tensor polarizability $\alpha_2^{(3)}$ is related to η_z by Eq. (5). In the M_x geometry, on the other hand, for which the pumping direction and the magnetic field direction, i.e., the axis of quantization, are no longer parallel this simple relation no longer holds. As a consequence oscillating steady state populations appear in all $2F+1|F=4,M\rangle$ states. This is illustrated in Figs. 8(a) and 8(b) where we compare the steady state populations produced by optical pumping of the sublevels in the $F=4$ manifold in the M_z and in the M_x geometries, respectively. These results were obtained from a rate equation calculation described earlier [15]. The parameters of that calculation are the optical pumping rate, γ_p, proportional to the laser intensity, and the longitudinal spin relaxation rate, γ_1.

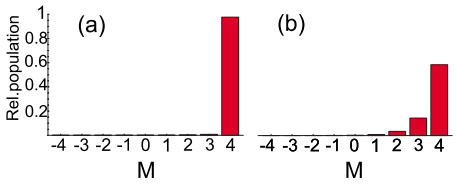

FIG. 8. (Color online) Steady state populations after optical pumping in the ground state level $F=4$ in the M_z configuration (a) and in the M_x configuration (b). The parameters (defined in [15]) of the calculation are the pumping rate $\gamma_p = 2500\ \text{s}^{-1}$ and the longitudinal spin relaxation time $\gamma_1 = 1\ \text{s}^{-1}$.

V. ANALYSIS OF THE M_x DATA

Because of the tilted quantization axis the extraction of the tensor polarizability $\alpha_2^{(3)}$ from the data of Fig. 7 recorded in the M_x geometry requires a more detailed analysis. We base this analysis on the three step approach, discussed in [18], which is well-suited for the quantitative description of optically detected magnetic resonance signals. In that model the double resonance process is treated as three time sequential processes, viz., the creation of steady state spin orientation by optical pumping, the evolution of that initial orientation under the influence of the external fields, and finally the optical detection of the steady state oscillation reached in the second step. The validity of this approach is discussed in the quoted reference.

A. The optical pumping process (step 1)

In the first step spin polarization (orientation) is created in the sample by optical pumping with circularly polarized resonance radiation. The interaction with the magnetic field and relaxation processes then lead to a steady state redistribution of the sublevel populations p_M, as shown in Fig. 8 for a given set of the parameters γ_p and γ_1. For the calculation one sets the quantization axis along the static field $\vec{B}_0$, and the populations produced in the first step are expressed in this coordinate system.

B. The magnetic resonance process (step 2)

In the magnetic resonance process the initial spin orientation evolves to a steady state precession under the joint action of the external fields $\vec{B}_0$ and $\vec{B}_1 \cos\omega_{rf} t$ and of relaxation. This evolution is described by the Liouville equation for the density matrix ρ

$$\dot{\rho} = -\frac{i}{\hbar}[H(t),\rho] + H_{\text{relax}}. \tag{11}$$

After applying the rotating wave (rw) approximation (coordinate system rotating at the frequency ω_{rf} around $\hat{B}_0$) the Hamiltonian becomes time independent and reads

$$H = \omega_L F_z - \Omega_R F_x, \tag{12}$$

where $\omega_L = \gamma_F B_0$ and $\Omega_R = \gamma_F B_1/2$ are the Larmor and Rabi frequencies, respectively (γ_F is the Landé g-factor of the level F).

By considering the hyperfine level $F=4$ only and after introducing longitudinal and transverse relaxation rates γ_1 and γ_2, one obtains nine equations for the time evolution of the populations

$$\dot{p}_M = \dot{\rho}_{M,M} = -iV_{M,M+1}(\rho_{M+1,M} - \rho_{M,M+1}) - iV_{M,M-1}(\rho_{M-1,M} - \rho_{M,M-1}) - \gamma_1(\rho_{M,M} - \rho^0_{M,M}), \tag{13}$$

where $V_{M,M'} = \langle 4, M|\Omega_R F_x|4, M'\rangle$ and $p^0_M = \rho^0_{M,M}$ are the steady state populations produced by the optical pumping in step 1, and eight additional equations for the coherences

$$\dot{\rho}_{M,M-1} = -i\delta\omega\rho_{M,M-1} - iV(\rho_{M-1,M-1} - \rho_{M,M}) - \gamma_2\rho_{M,M-1}, \tag{14}$$

where $M=-3,\ldots,4$ and $\delta\omega=\omega_L-\omega_{rf}$ is the detuning. With the complex conjugates of Eq. (14), the dynamics are then described by a system of 25 differential equations, which allow us to calculate numerically the steady state populations p_M and coherences $\rho_{M,M\pm1}$. When transforming back from the rw system to the laboratory frame the $\Delta M=\pm1$ coherences $\rho_{M,M\pm1}$ will oscillate like $\exp[\pm i\omega_{rf}t]$.

C. The optical detection (step 3)

In the third step one calculates the fluorescence rate produced by absorption of the circularly polarized laser beam by the medium described by the steady state density matrix obtained in step 2. The time dependent signals oscillating at ω_{rf} are determined by the $\Delta M=\pm1$ coherences $\rho_{M,M\mp1}$. Their contribution to the absorption signal is given by

$$S_{M,M-1} \propto \mathrm{Re}\left[\sum_{f,m}\langle m|\mathbf{d}\cdot\mathbf{e}|M\rangle\rho_{M,M-1}\langle M-1|(\mathbf{d}\cdot\mathbf{e})^\dagger|m\rangle\right], \tag{15}$$

where $\mathbf{d}$ is the electric dipole operator and $\mathbf{e}$ the optical field vector. The state vectors $|M\rangle$ and $|m\rangle$ denote the states $|6S_{1/2},F,M\rangle$ and $|6P_{1/2},f,m\rangle$, respectively.

The effect of the tensor polarizability is taken into account by adding the differential Stark shift of the levels $|M\rangle$ and $|M-1\rangle$ to the detuning via

$$\delta = \omega_L - \omega_{rf} + \frac{3}{56}(2M-1)\alpha_2^{(3)}\mathbb{E}^2. \tag{16}$$

In this way one can calculate the absorptive and dispersive resonance signals in the M_x geometry by adding the contributions of all the individual transitions

$$S_{\mathrm{tot}}(\delta) = \sum_M S_{M,M-1}(\delta). \tag{17}$$

The equivalent signals obtained in the M_z geometry can be calculated in an analogous way by assuming all of the initial population to be concentrated in the $|4, 4\rangle$ state. In Fig. 9 we compare the effect of an electric field of 40 kV/cm on the magnetic resonance spectra recorded in the M_z and in the M_x geometries for a particular set of the parameters, $\gamma_1=1\ \mathrm{s}^{-1}$, $\gamma_2=4\ \mathrm{s}^{-1}$, $\gamma_p=2500\ \mathrm{s}^{-1}$ [13,15], and $\Omega_R=50\ \mathrm{s}^{-1}$ (corresponding to $B_1\approx4.5$ nT). One sees that in this case the Stark shift obtained in the M_x geometry is reduced by a factor ϵ, which, for the set of parameters $\gamma_p=2500\ \mathrm{s}^{-1}$ and $\Omega_R=50\ \mathrm{s}^{-1}$ has the value $\epsilon=19.2\ \mathrm{Hz}/5.5\ \mathrm{Hz}=3.49$. We take this reduced sensitivity into account by writing the electric field dependence of the Stark shift in the M_x geometry, in analogy to Eq. (5), as

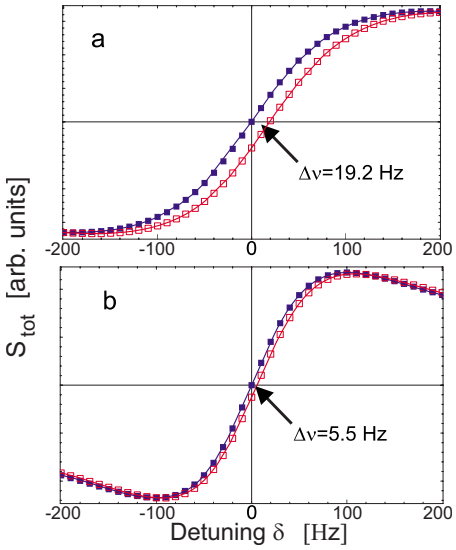

FIG. 9. (Color online) Calculated resonance signal produced by (a) the single magnetic transition $|4,4\rangle\rightarrow|4,3\rangle$ in the case $\beta=0$, and (b) the sum of all magnetic transitions $|M\rangle\rightarrow|M-1\rangle$ for the case $\beta=\pi/4$. Filled squares represent the $E=0$ case, while empty squares give the magnetic resonance line shape in an electric field of 40 kV/cm. For the numerical calculations we have assumed $\alpha_2^{(3)}=-3.49\times10^{-2}\ \mathrm{Hz}/(\mathrm{kV/cm})^2$, which is a weighted average of previous measurements. The other parameters are $\gamma_p=2500\ \mathrm{s}^{-1}$, $\gamma_1=1\ \mathrm{s}^{-1}$, $\gamma_2=4\ \mathrm{s}^{-1}$, and $\Omega_R=50\ \mathrm{s}^{-1}$. Note that the different widths of (a) and (b) are consequences of different power broadenings of the single magnetic resonances.

$$\Delta\nu_4 = \eta_x\mathbb{E}^2 = -\frac{3}{8}\frac{1}{\epsilon}\alpha_2^{(3)}(4)\mathbb{E}^2, \tag{18}$$

or, equivalently

$$\alpha_2^{(3)}(4) = -\frac{8}{3}\epsilon\eta_x. \tag{19}$$

In this way we obtain from Eq. (10)

$$\alpha_2^{(3)}(4) = (-4.36\pm0.28)\times10^{-2}\frac{\mathrm{Hz}}{(\mathrm{kV/cm})^2}. \tag{20}$$

This value is shown in Fig. 11 as point (e). It is in good agreement with the experimental result obtained in the M_z geometry (point d). The error bar of point (e) takes a slight uncertainty of the correction factor ϵ into account. The value of ϵ used above was obtained using our best possible estimation of the experimental parameters γ_p and Ω_R. In order to check the sensitivity of ϵ to the uncertainties of these parameters we have varied the parameters in the simulation calculation. The results shown in Fig. 10 indicate that ϵ is rather

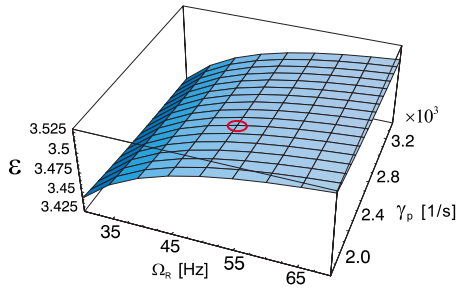

FIG. 10. (Color online) Correction factor ϵ as a function of the relevant parameters γ_p and Ω_R. The circle shows the parameters used to produce Fig. 9.

insensitive to parameter variations. A change of the Rabi frequency by ±50% changes ϵ by approximately 3%, while a change of the pumping rate γ_p by ±50% changes ϵ by 0.8%. We have taken this uncertainty into account by assigning a (conservative) uncertainty of 1% to ϵ, a value which does not affect the error given in Eq. (20).

VI. COMPARISON WITH THEORY

Recently we have shown [8] that the inclusion of off-diagonal hyperfine matrix elements in the third order theory of forbidden tensor polarizabilities leads to a good agreement between experimental and theoretical values in the case of free Cs atoms. The present experiments show that the modulus of the tensor polarizability of Cs in solid He is approximately 10% larger than the corresponding vacuum value (Fig. 11). This is due to the interaction of the Cs atom with the He matrix which affects both the Cs energies and wave functions entering the third order perturbation theory. We have therefore extended our tensor polarizability calculations by including the effect of the helium matrix [9] in the frame of the so-called extended atomic bubble model [12]. The result of that calculation (details of which will be presented elsewhere [9]) is shown on the right side of Fig. 11 as a dashed line and shows an excellent agreement with the experimental results presented above.

VII. SUMMARY

We have performed the first measurement of the Stark effect in the ground state of Cs atoms implanted in a solid

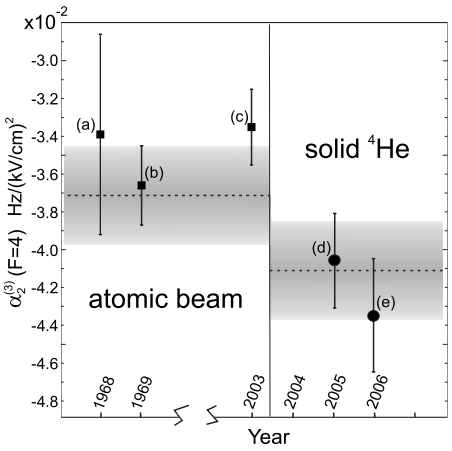

FIG. 11. The Cs tensor polarizability $\alpha_2^{(3)}(F{=}4)$. Atomic beam measurements of (a) Carrico *et al.* [4], (b) Gould *et al.* [5], and (c) Ospelkaus *et al.* [6]. Points (d) and (e) represent the measurements in solid helium, in the M_z and M_x geometries, respectively, reported in this work. The dashed lines are the theoretical values for the free atom [8] and for Cs in a solid helium matrix [9], together with their uncertainties (shaded bands).

^{4}He matrix [19]. Measurements performed in two different experimental configurations have yielded consistent values for the forbidden tensor polarizability. The experimental results are well-described by a bubble model calculation and show that the helium matrix changes the tensor polarizability by approximately 10%.

We have also measured the relative sign of the polarizabilities in the two hyperfine levels. The experimental result agrees with our theoretical prediction and is in contradiction with the sign predicted by a previous calculation. This confirms the need [8] for a reevaluation of the dynamic Stark shift of primary frequency standards induced by the blackbody radiation field [20], when this effect is inferred from static Stark shift measurements as done, e.g., by Simon *et al.* [21].

ACKNOWLEDGMENTS

We acknowledge the skillful help of Stephan Gröger for the measurements in the M_x geometry. This work was supported by Grant No. 200020-103864 of the Swiss National Science Foundation.

[1] J. R. P. Angel and P. G. H. Sandars, Proc. R. Soc. London, Ser. A **305**, 125 (1968).
[2] R. D. Haun and J. R. Zacharias, Phys. Rev. **107**, 107 (1957).
[3] E. Lipworth and P. G. H. Sandars, Phys. Rev. Lett. **13**, 716 (1964).
[4] J. P. Carrico, A. Adler, M. R. Baker, S. Legowski, E. Lipworth, P. G. H. Sandars, T. S. Stein, and C. Weisskopf, Phys. Rev. **170**, 64 (1968).
[5] H. Gould, E. Lipworth, and M. C. Weisskopf, Phys. Rev. **188**, 24 (1969).
[6] C. Ospelkaus, U. Rasbach, and A. Weis, Phys. Rev. A **67**, 011402(R) (2003).
[7] P. G. H. Sandars, Proc. Phys. Soc. London **92**, 857 (1967).
[8] S. Ulzega, A. Hofer, P. Moroshkin, and A. Weis, Europhys. Lett. **76**, 1074 (2006).
[9] A. Hofer, P. Moroshkin, S. Ulzega, and A. Weis (unpublished).
[10] M. Arndt, S. I. Kanorsky, A. Weis, and T. W. Hänsch, Phys. Lett. A **174**, 298 (1993).
[11] A. Weis, S. Kanorsky, S. Lang, and T. W. Hänsch, in *Atomic Physics Methods in Modern Research*, Lecture Notes in Physics Vol. 499 (Springer, Berlin, 1997), pp. 57–75.
[12] P. Moroshkin, A. Hofer, S. Ulzega, and A. Weis, Low Temp.

Phys. **32**, 1297 (2006).
[13] M. Arndt, S. I. Kanorsky, A. Weis, and T. W. Hänsch, Phys. Rev. Lett. **74**, 1359 (1995).
[14] S. I. Kanorsky, S. Lang, S. Lücke, S. B. Ross, T. W. Hänsch, and A. Weis, Phys. Rev. A **54**, R1010 (1996).
[15] S. Lang, S. Kanorsky, T. Eichler, R. Müller-Siebert, T. W. Hänsch, and A. Weis, Phys. Rev. A **60**, 3867 (1999).
[16] R. Muller-Siebert, Ph.D. thesis, University of Fribourg, Switzerland, 2003 (unpublished).
[17] S. Gröger, G. Bison, J. L. Schenker, R. Wynands, and A. Weis, Eur. Phys. J. D **38**, 239 (2006).
[18] D. Budker, W. Gawlik, D. F. Kimball, S. M. Rochester, V. V. Yashchuk, and A. Weis, Rev. Mod. Phys. **74**, 1153 (2002).
[19] A preliminary analysis of the data discussed here was shown in [8]. That analysis did not take the thermal expansion of the field plate spacing into account.
[20] W. M. Itano, L. L. Lewis, and D. J. Wineland, Phys. Rev. A **25**, 1233 (1982).
[21] E. Simon, P. Laurent, and A. Clairon, Phys. Rev. A **57**, 436 (1998).